IAC-20, A7, 3, 7, x57894

Wavelength Calibration of the Full-sun Ultraviolet Rocket SpecTrograph (FURST)

Nicolas Donders ^{a,b}, Amy Winebarger ^c, Charles Kankelborg ^d, Genevieve Vigil ^c, Laurel Rachmeler ^e, Ken Kobayashi ^c, Gary Zank ^{a,b}

- ^a Department of Space Science, University of Alabama in Huntsville
- ^b Center for Space Plasma and Aeronomic Research, University of Alabama in Huntsville
- ^c Marshall Space Flight Center, NASA, Huntsville AL
- ^d Solar Group, Department of Physics, Montana State University, Bozeman MT
- ^e National Centers for Environmental Information, NOAA, Boulder CO

Abstract

The Sun has a well-known periodicity in sunspot number and magnetic field variation. The underlying cause of this 11-year cycle is not fully understood and has yet to be connected with those processes in other stellar objects. The Full-sun Ultraviolet Rocket SpecTrograph (FURST) is a sounding rocket payload being developed by Montana State University (MSU) alongside the Marshall Space Flight Center (MSFC) solar physics group. Scheduled to launch from White Sands Missile Range (WSMR) in 2022, this instrument is unique in that it will provide the connection between stellar observatories with measurements of our Sun. It will achieve this through measuring high-resolution full-disk spectral irradiance. We aim to obtain a wavelength resolution R > 10,000 in the 120 - 181 nm UltraViolet (UV) range, on par with that of the Hubble (HST) Space Telescope Imaging Spectrograph (STIS). This resolution goal will allow us to study the relatively low-temperature plasma in the chromosphere and lower corona with spectral accuracy down to 0.1 Å (a Doppler-shift of about \pm 30 km/s). In addition, the Lyman Alpha (121 nm) line is known to saturate most CCD electronics. These factors illustrate the particular challenge of precise wavelength calibration for this spectral range. We are building a collimator in order to calibrate the FURST instrument under these strict spectral requirements. This paper will present the results of our simulation of the diagnostic lamp signal to be used for wavelength calibration. The simulation allows us to begin to account for photon noise, electronic readout noise, and statistical error. These in turn lead to the development of our pre- and post-launch calibration plans. Future work includes absolute radiometric and wavelength calibration with this new collimator. In addition, the ability of FURST to measure small Doppler-shifts will provide capabilities for planetary atmospheric scientists. This impact is coupled with the diverse international partnership created by the closely-knit Sounding Rocket teams around the globe. Sounding Rockets like FURST have an even broader impact, as they encourage future satellite missions under the prospect of long-term observations.

1 Introduction

The Sounding Rocket team at NASA's Marshall Space Flight Center (MSFC) have been producing unique optical experiments as part of the Solar Physics group [Tsuneta et al., 2008, Kano et al., 2012, Ishikawa et al., 2017]. While some current missions are set to look at X-rays (MaGIXS, Kobayashi et al. [2018]), and others will study active flaring regions (Hi-C Flare, see Kobayashi et al. [2014] and Winebarger et al. [2019]), the Full-sun Ultraviolet Rocket Spectrograph (FURST) is different [Kankelborg et al., 2017].

It is foremost a partnership between MSFC and Montana State University (MSU). The focus for this payload is to produce a full-disk spectral image in the Vacuum UltraViolet (VUV) range, specifically between 1200 - 1810 Å. This wavelength region in-

cludes many important energy lines, such as Lyman Alpha ≈ 1215.67 Å. This line in particular is extremely bright, raising concern of CCD saturation for full disk measurements. Additionally, the resolution goals of FURST far outpace the data currently available. Such spectral lines have been well characterized in other stars by missions like the Hubble Space Telescope (HST). While FURST aims for a resolution R > 10,000 (< 30 km/s), solar data from HST over this VUV range has an R $\approx 1,000$ (300 km/s) [Woods et al., 2010]. To make matters more convincing, higher resolution data (R $\approx 17,000$, ≈ 18 km/s) only covers few Angstroms with large gaps between them [Peter, 1999, Wilhelm et al., 1995].

In order to achieve these resolution goals, the FURST instrument has some unique optical characteristics. A typical spectrograph utilizes a slit aperture open to a grating mirror. The FURST instru-

IAC-20,A7,3,7,x57894 Page 1 of 8

ment instead takes in a full-disk image and creates a virtual slit by way of optical cylinders. Figure 1 shows the light-path through the instrument design, as per Kankelborg et al. [2017].

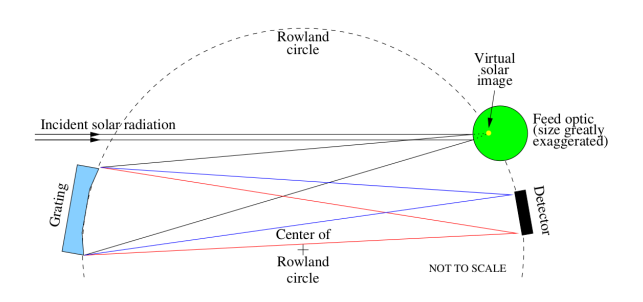


Figure 1: From Kankelborg et al. [2017]: "Conceptual sketch of optical design."

Referring to Figure 1, each of the optical cylinders are placed precisely around the Rowland circle, such that they reflect towards the grating and then the CCD. To cover the desired 610 Å range with high precision, there are seven optical cylinders combined with a shutter system which reflect ≈ 104 Å at a time towards the grating. When the experiments are performed, the photon signal received at the detector is translated as an electronic transmission and subsequently converted to an intensity in Data Numbers (DN) at each pixel.

Mapping every pixel to its corresponding wavelength requires calibration prior to the experiment. To do this we rely on a well known diagnostic lamp source [Sansonetti et al., 2004]. This Pt/Cr-Ne lamp shows the Gaussian-shaped spectral lines of the elements within. The lab-based measurements are reliable for calibration, but don't highlight the turbulent and messy nature of the actual solar plasma. However, based on the physical and chemical properties of the plasma we can compare the differences between the width and location of these Gaussian curves with respect to their expected / theoretical values. This will help to answer a key science goal, since this difference is caused by Doppler-shifts (due to plasma velocity and solar rotation) and thermal broadening (due to magnetic and turbulent activity). Thus, it becomes imperative to know the expected location of the spectral lines so that we can functionally map each pixel number to a specific wavelength. This function is further complicated due to fluctuations in the expected number of incident number of photons, electronic "dark noise," and readout error, among other sources. Tabulated in Table 1 is a short list of a few likely contributors to be considered herein.

Component	Issue	Impacts	Manage By	Predicted Impact	Estimated Error
Lamp Calibration	Absolute Wavelength Accuracy	Wavelength Error	NIST	Small	±0.002 Å
	Absolute Radiometric Accuracy	Intensity Error	NIST	Negligible	±? W/cm^2/sr
Camera	Electron Noise	SNR	Simulation Estimates, Integration Time	Medium	±25 Electrons
	Photon Noise	SNR	Averaging	Small	Poisson
Simulation	Curve Fitting (Gaussian)	Relative Wavelength Calibration	Improved Fitting Procedures	Negligible	±10^-8 pixels
	Curve Fitting (Orthogonal Distance Regression)	Relative Wavelength Calibration	Calibration of Diagnostic Lines, Instrument Response Function	Medium	±0.06 Å (±12 km/s)

Table 1: Summary of known or estimated sources of error and their management strategies.

As the Table highlights, for our analysis we must first consider all reasonable sources of error so that we can account for them as we model and improve this simulation. This paper begins by explains how our code generates the simulated signal using a NIST calibrated lamp [Sansonetti et al., 2004]. We then map the incident photon signal onto a detector array by way of a line-spread function. Since the number of photons is a countable source, we have to introduce Poisson error. In addition, converting the signal from number of photons to an electronic readout introduces readout noise. The conversion from electons to DNs is modulated by a Gain factor. This factor is another source of modulation of the signal, and the analysis of this will be covered in an upcoming SPEI paper [Vigil et al., 2020].

After the simulated signal at each pixel has been generated with these errors, we perform Gaussian curve-fitting on a few select lines to obtain sub-pixel resolution. This is done for the ranges covered by each feed optic. We generate the simulated signal multiple times in a Monte-Carlo fashion. This method gives more precision, since we can employ the standard error of the mean from the resulting histograms. Finally, we use this data to generate the mapping function for each range using a second-order polynomial Orthogonal Distance Regression (ODR) method. This takes into account the estimated error in pixel number (from the simulation) and the error in wavelength (based on the diagnostic lamp calibration) For a result, we look at the propagation of error in the function parameters to judge our success in reaching the resolution goals. A summary of these is provided in Table 1 above, with estimates provided.

IAC-20,A7,3,7,x57894 Page 2 of 8

2 Generating and Mapping the Simulated Signal

The diagnostic signal used in this characterization is a Pt/Cr-Ne lamp from Sansonetti et al. [2004]. The lamp produces a signal based on the voltage supplied (see paper sources), see Figure 2.

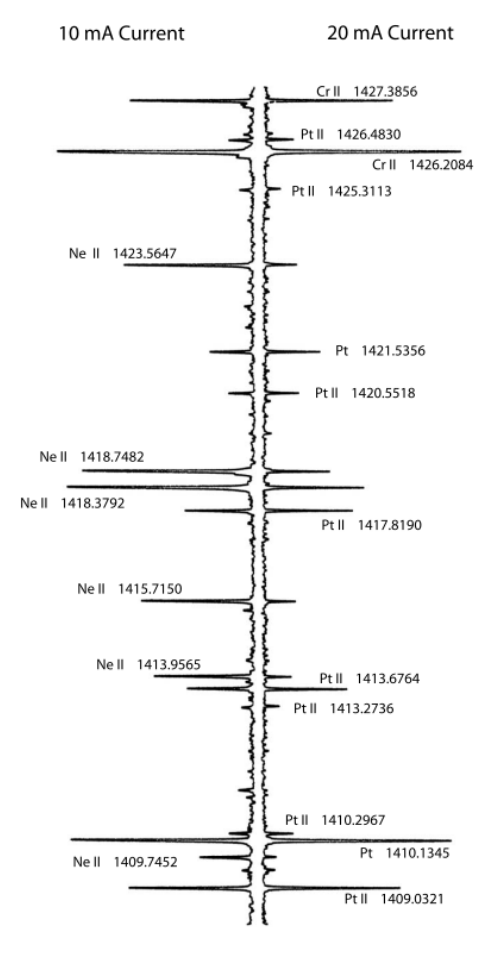


Figure 2: From Sansonetti et al. [2004]: "Tracings of the spectrum of a Pt/Cr-Ne hollow cathode lamp operated at 10 mA (left) and 20 mA (right) around 1420 Å. Lines of different species are identified with wavelengths given in Å. Note that all Ne II lines are enhanced relative to the Pt II in the 10 mA spectrum".

For this simulation, we choose the 20 mA signal (right). The lines of a few species are identified here as well. Though the plot only shows wavelengths 1409 - 1427 Å, the reference paper covers calibration between 1132 - 1828 Å. This will cover our desired range of 1200 - 1810 Å. Treating the file to remove extraneous characters and delimiters, we find that the data only gives the line locations and intensity. Thus, we must give the signal a realistic Gaussian width based

on physical properties. We start with the basic formula for a Gaussian in the presence of a uniform background:

$$I = (I_0 - I_b) e^{-\frac{(\lambda - \lambda_0)^2}{2\sigma^2}} + I_b \tag{1}$$

, where I is the amplitude of the peak intensity I_0 and the background I_b , λ is the wavelength and mean wavelength of the peak λ_0 , and σ is the width. The width σ is of particular interest here. One of the physical reasons for the spectral line having a width is the instrument response function σ_{width} . This spectral spreading is defined by the line-spread function of the instrument. For now, we set the width through linear interpolation between three experimentally determined points:

$$\sigma_{width} = \begin{cases} 0.019 \text{ Å} & \text{if} \quad \lambda = 1170 \text{ Å} \\ 0.026 \text{ Å} & \text{if} \quad \lambda = 1570 \text{ Å} \\ 0.039 \text{ Å} & \text{if} \quad \lambda = 1960 \text{ Å} \end{cases}$$
 (2)

As this project progresses, we aim to have a measured instrument response function data at more discrete intervals across the spectral range. This will allow for a more dynamic simulation. Additionally, simulating this signal requires us to set up a matrix for the Gaussian to map to. At the moment, we are assuming linearity in this mapping a priori. Eventually, it will become necessary to assign a non-linearity. This can be done by accounting for factors such as how the grating will spread the signal, the angle of incidence, etc. This can be done, although it is not so important at this stage. Surely there will be many other sources of error in how the signal reaches the detector, but for now we simply want to look at how a signal of any kind is interpreted, and the resulting error in our ability to do so. Thus, we have inherently assigned linearity to the mapping, and we will see how well we can estimate this.

Continuing with the formulae above, we map the signal as transmitted by each cylinder into pixels. This is most easily done by using an array of size equal to that of the CCD array. Therefore, the signal is mapped to discrete points instead of as a continuum. Figure 3 (left) shows those mapped intensities from the lamp data, covering the 7 wavelength ranges needed between the full range of 1200 - 1810 Å. Firstly, note how this Gaussian has been mapped onto discrete pixels (right plot). As the black lines indicate, the exact location of each peak will most likely be in between pixels. Using this fact, the next section of this paper will discuss the use of a Gaussian fit to obtain sub-pixel precision for these locations. The FURST instrument design achieves the high level of resolution due in part to this multi-cylinder design.

IAC-20,A7,3,7,x57894 Page 3 of 8

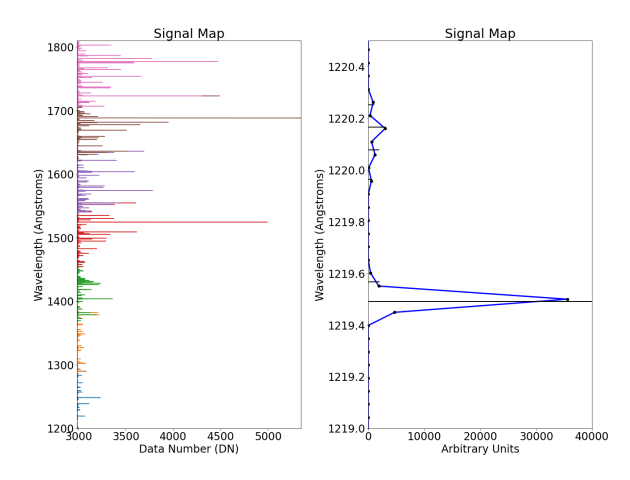


Figure 3: Lamp data in the 1200-1810 Å range relevant to FURST, in arbitrary units. Left: The signal received by each of the cylinders. Right: The zoomed figure indicated with markers to show the discrete nature of the pixel array. The horizontal bars provide a representation of where the original signal was located before this mapping, as well as and it's intensity.

Each cylinder is able to transmit a certain range of wavelengths to the detector. Figure 3 (left) shows how we have designed these ranges such that there is enough overlap to cover the full spectrum range. In reality, these ranges and overlaps may not be equal. For now, this simulation does not take this variability into account, nor does it assume non-linear mapping at this stage, but these can easily be modified in the future to do so. Secondly, these two plots show the intensity in arbitrary units. There is a conversion process to obtain the signal in Data Numbers (DNs). In order to do this, we have to take into account the effective area and the various sources of noise.

3 Converting the Signal to Real Units

To convert the signal intensity to real units, we use the given conversion rate of $2 \cdot 10^{10}$ W cm⁻² sr⁻¹ per arbitrary unit. Multiplying this number by the effective area gives the intensity in W/sr. The effective area is calculated using interpolated values given by the manufacturer of the coatings and mirrors, etc. In the following figure, we show the Effective Area of the FURST instrument. This is a multiplication of the quantum efficiency of the detector, the transmission of the filters, and the reflectivity of the mirrors, cylinders, and grating. We also account for additional factors including reflection of two mirrors in the col-

limator. In addition, we only consider a single row of the CCD. This means that the intensity is further reduced by the fact that the light is smeared across 1024 pixels. In practice, we would have higher-resolution data from all of these manufacturers, along with associated error.

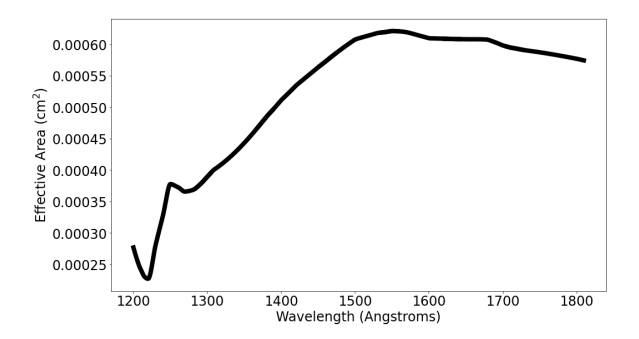


Figure 4: Effective Area of the FURST instrument and Collimator.

Using this calculated effective area from Figure 4, we convert the signal into Watts per steradian. Since each pixel sees about $10 \cdot 10^{-6}$ sr, we convert the intensity to be in Watts. We can then divide by the energy per photon (given by $E = hc / \lambda$) to find the intensity in photons per second. We can also adjust the exposure time and total number of exposures. For now, we use the estimate of 10 seconds and 10 exposures in total. This gives the intensity in photons. From here, we add photon noise in an Monte-Carlolike fashion, which will be discussed later on. Next, dividing by the electron energy $1.602 \cdot 10^{-19}$ (J/electron) we can convert the intensity in photons to electrons. From here, we can add real noise to the electron signal. The photon noise, electronic readout noise, and data-number (DN) bias are all part of a Monte-Carlo loop.

4 Monte-Carlo Gaussian-Fitting

As described in the introduction, the mapping function requires knowledge of the expected location of each peak in terms of pixel number. We used a Gaussian function to add line-spreading to each peak. In the process of converting to real units, Ww need to account for random noise, namely discrete Poisson noise and electronic readout noise.

Since the CCD is recording a photon count rate, Poisson noise is added to the signal once it is converted to photons. Then after converting to electrons we add a readout noise of $25~\mathrm{e}^-$. This is because the

IAC-20,A7,3,7,x57894 Page 4 of 8

electronic signal transmission is read by the computer from the CCD. It is read at a gain of 1 DN per e⁻ with a bias of 3000 DN. To account for randomness, this is performed in a Monte-Carlo fashion: we add this noise within a loop, and then attempt to recompute the location of the line using a Gaussian curve-fit.

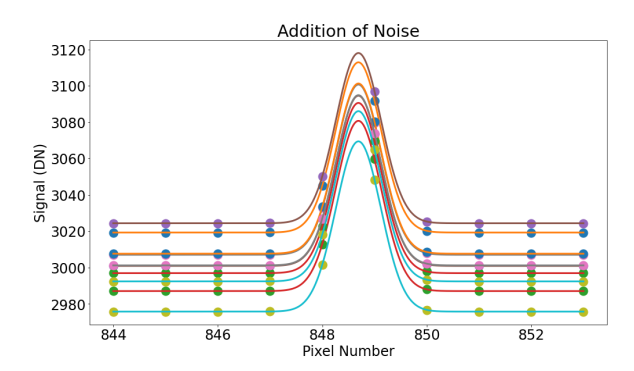


Figure 5: Example of multiple simulated signals converted to Data Numbers (DNs), with the addition of photon noise, electronic readout noise, and DN bias. The Gaussian curve highlights the sub-pixel resolution obtainable through fitting.

Figure 5 shows multiple simulated signals overlayed. Here they have been converted to DN as described above. This curve-fitting function is written in the same form as Equation 1, and is fit using Python's "scipy.optimize.curve_fit" package. The peak location is resolved from this fitting with subpixel resolution.

These sub-pixel-resolution results will be obtained for each exposure. After the addition of noise is repeated several times, the error in this measurement is calculated based on the standard error of the mean as follows.

$$\sigma_M = \sigma/N \tag{3}$$

, where σ is the usual standard deviation and N is the number of exposures. Thus, the more exposures N that we take during calibration, the more confident we can be about the location of these peaks. This gives us a mean location for each peak with the associated error in our knowledge in that peak. Using the standard error of the mean is vital for this experiment, since the actual science data may only offer around 10 exposures during flight.

For each cylinder's wavelength range, we previously identified the top 5 peaks to use as diagnostic lines. For the simulation here, using this knowledge allows us to provide an estimate for these pixel locations, widths, backgrounds, and amplitudes. In practice, we will be much more precise about which specific lines we use. In doing so we will be taking into

account other factors, such as their spacing throughout the specific range and the reliability of the diagnostic lamp.

So, the better we can mitigate any such errors associated with calibration, the more we can focus on those other sources. This Monte-Carlo routine is then repeated across the input signals from each cylinder. Now, we have provided simulated data that can be used to directly correlate pixel number to wavelength number. Using a different kind of curve-fitting, the next section will discuss this numerical relation. From here we will only focus on the five most intense source lines from each cylinder range.

5 Fitting Wavelength vs. Pixel

The final stage of this simulation is to find the best-fit the functions for directly correlating pixel number to wavelength. This time, the curve-fitting must take into account the error in both pixel number and wavelength values. To do this we utilize the "scipy.odr" package, which containes an Orthogonal Distance Regression algorithm. For now we have defined the function as a simple 2nd order polynomial of the form

$$\lambda = (\lambda_0 \pm \Delta \lambda_0) + (A \pm \Delta A) \cdot x + (B \pm \Delta B) \cdot x^2 \quad (4)$$

, where x is the pixel value, and the parameters λ (Å), A (Å/pixel), and B (Å/pixel²) are supplied with their associated error.

Each of these 7 optical signals will have unique mapping functions based on the geometry, reflectivity, etc, and may not be as similar as they are here. In addition, our current mapping is mostly linear. As mentioned before, this assumption was inherently assumed based on the way the signal was simulated. However, accounting for this possibility now will allow us to account for it later on when the experimental results show otherwise. Below are listed the error results from a single run, with 10 exposures of 5 lines per cylinder range.

IAC-20,A7,3,7,x57894 Page 5 of 8

Cylinder #	$\Delta \lambda_0$	$\Delta A \cdot 10^{-5}$	$\Delta B \cdot 10^{-8}$
1	0.0181	3.57	1.43
2	0.0137	3.40	1.63
3	0.0102	2.80	1.81
4	0.0476	6.87	2.37
5	0.0319	6.55	2.74
6	0.0315	5.80	2.43
7	0.0049	1.21	0.65
Mean	0.0226	4.31	1.87

Table 2: The polynomial correlation at each signal as found by the Orthogonal Distance Regression (ODR) method.

The error in numbers 1, 2, 3, and 7 appear to be quite low. However, cylinders 4, 5, and 6 seem to have higher errors for the Δ terms. This may have been attributed to the nature of the spectral lines within that wavelength range. Looking back at Figure 3, the red and brown lines of cylinders 4 and 6 only appear to have a few clearly distinct and separate lines. This may result in the diagnostic signals to be rather messy for those chosen lines. Thus, special care in choosing diagnostic signals will be taken here in future experimental practice.

Next, analysis of these results is better suited in the form of Resolution R.

$$R = \frac{\lambda}{\Delta \lambda} = \frac{c}{\Delta v} \implies \Delta v = c \frac{\Delta \lambda}{\lambda} = \frac{c}{R}$$
 (5)

, where Δv is the Doppler-shift resolution of the wavelength. As mentioned in the introduction, our goal is an R > 10,000. In our wavelength range (1200 - 1810 Å), this corresponds to a goal of < 0.120 - 0.181 Å in resolution, or \approx 30 km/s. Using the propagation of error, the polynomial in equation 4 gives us $\Delta\lambda$ as

$$\Delta \lambda = \sqrt{\Delta \lambda_0^2 + (\Delta A \cdot x)^2 + (\Delta B \cdot x^2)^2}$$
 (6)

, where x is evaluated at pixel number 1 and 2048. If we calculate these values line-by-line, we can find the resolution Δv of each cylinder's range.

Range (Å)	$\Delta\lambda$ (Å)	$\Delta v \; (\mathrm{km/s})$
1200.0 - 1304.0	0.018 - 0.098	4.55 - 22.5
1284.3 - 1388.3	0.014 - 0.110	3.28 - 23.8
1368.7 - 1472.7	0.010 - 0.101	2.36 - 20.5
1453.0 - 1557.0	0.048 - 0.185	9.85 - 35.7
1537.3 - 1641.3	0.027 - 0.151	5.27 - 27.5
1621.7 - 1725.7	0.031 - 0.150	5.69 - 26.1
1706.0 - 1810.0	0.004 - 0.036	0.79 - 6.02
Mean	0.058	11.6

Table 3: Resolution Δv for each cylinder's range, rounded for simplicity.

To summarize Table 3, the Δv resolution we can obtain will most likely be between ≈ 1 - 40 km/s, with a mean value around 11-12 km/s. This mean is skewed though, due to the rise in error towards the one end of the CCD. This is more easily visualized on the following plot from another run of the simulation.

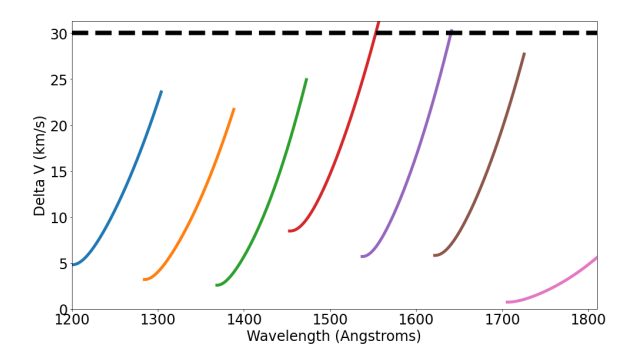


Figure 6: Δv Resolution across the CCD from each exposure range. The goal of 30 km/s is shown by the dashed line.

This figure highlights the effects of propagation of error in terms of our resolution goals. As the error propagation increases towards the higher pixelvalues, the goal of 30 km/s is sometimes over-passed. Based on many runs of this simulation, the variations seen in this resolution result are small but sometimes different lines cross the goal-line. However, two things should be noted here. For one, the overlap between the spectral ranges of the different cylinders should allow us to use information from the two signal together. In other words, the high-error end of each line in the figure is offset by the low-error end of the signal from the next cylinder. Secondly, we are only considering one row of pixels here. In practice, we should be able to get better statistics by looking at the mapping across every row together. Thus, given proper diagnostic techniques, the given setup should allow us to be able to resolve the signal within the 30 km/s resolution goal.

The possibility of resolving down to 30 km/s is definitely possible for most parts of the CCD. If we want to be more ambitious, though, we will have to make further improvements or change our fitting scheme in order to improve this resolution. For example, artificially lowering the pixel and wavelength errors that go into this fitting will not necessarily improve the resulting resolution values. However, if we choose to use 4 diagnostic lines instead of 5, then the mean Δv drops to around 7 km/s (0.2 - 36 km/s). It should be noted that fitting a 2nd order polynomial with only 4 points will give a perfect correlation. This means that an average error of \approx 7 km/s

IAC-20,A7,3,7,x57894 Page 6 of 8

can be thought of as a lower bound for this measurement. What's more, the initial mapping of the signal was done in an implicit linearity. Dropping the nonlinear term in the regression, we obtain even better results. In this case, 5 diagnostic lines fit with a linear regression model yields an average resolution of ≈ 1 - 8 km/s. These few test cases show that for now our resolution goal is more than possible. We will discuss our a few other possible improvements in the final section, as well as other sources of error not yet accounted for.

6 Results and Conclusions

From a diagnostic lamp signal, adding in the sources of noise and accounting for the line-spread function of the instrument, we have developed a mapping function for converting from CCD pixels to Wavelength. Future work may consist of using this relationship in reverse, allowing us to take an input CCD signal, in terms of pixel number and Data Numbers (DNs), and map out the corresponding wavelengths and photon energies.

This simulation is a work in progress, as experimental values will change many of the parameters. Using propagation of error, we have determined that at present case, we will be able to achieve a Doppler-shift resolution of at least $\approx 40~\rm km/s$, but more likely around 12 km/s. In addition, we provided a few examples of how variations in the regression model or choice of diagnostic lines show potential areas for improvement in this statistic.

The goal resolution was set to be 30 km/s. With minor exception, the goal is achieved by this simulation. However, there is much room for improvements in our design and calibration process. This simple model accounted for the obvious sources of noise, but we have yet to touch on the others. Referring to the error summary from the introduction, Table 1, we have listed sources of error associated with the camera, diagnostic lamp and the simulation. Additionally, the effective area and line-spread function will be measured experimentally and will have associated error margins. This is especially necessary, since we will be building a new collimator to perform these calibrations.

One other area of follow up research will be in the experimental validation of our camera parameters such as gain. In this simulation, gain was set at a constant of 1 DN per e⁻. However, past experience has shown that this value is modulated by extraneous factors such as temperature, and even others that are not or cannot be monitored. In order to capture

this gain fluctuation, we are in the process of developing a program for an on-board radiation "control" measurement. Not only will we calibrate with a lab diagnostic signal such as this Pt/Cr-Ne lamp, we aim to monitor the gain with an Fe-55 radioactive source. This will give us increased accuracy and precision of the gain measurement, and thus improve the readout noise associated with that error. This future work will be discussed by our group in future publications such as Vigil et al. [2020].

In summary, this work has shown the potential of our FURST instrument to meet the resolution requirements it was designed to obtain. Our future work will consist of improving our modeling techniques, building a new and improved collimator for calibration, and gathering experimental data to validate that these and other requirements can be meet.

7 Acknowledgements

Credit should go first and foremost to Dr. Charles Kankelborg and the MSU team for coming up with this unique solution to this much overlooked problem.

Even more thanks go out to my research advisor, Dr. Amy Winebarger, for her many hours of guidance in giving me the opportunity to understand the crazy and exciting world of Sounding Rockets!

Many thanks to my academic advisor Dr. Gary Zank for pointing me in this direction and providing the funding necessary to do so.

Additionally, there are many people within the NASA MSFC Sounding Rocket team and the UAH Space Science Department who deserve gratitude for their help with this work and the many other projects.

As always, I could not do this without the love of God and the continual support from my wife and family.

Thank you!

This material is based upon work supported by the NSF EPSCoR RII-Track-1.2a (Non-invasive plasma diagnostics for LTP) Cooperative Agreement OIA-1655280. Any opinions, findings, and conclusions or recommendations expressed in this material are those of the authors and do not necessarily reflect the views of the National Science Foundation.

References

S Tsuneta, K Ichimoto, Y Katsukawa, S Nagata, M Otsubo, T Shimizu, Y Suematsu, M Nakagiri, M Noguchi, T Tarbell, et al. The solar optical telescope for the hinode mission: an overview. *Solar Physics*, 249(2):167–196, 2008.

IAC-20,A7,3,7,x57894 Page 7 of 8

- Ryouhei Kano, Takamasa Bando, Noriyuki Narukage, Ryoko Ishikawa, Saku Tsuneta, Yukio Katsukawa, Masahito Kubo, Shin-nosuke Ishikawa, Hirohisa Hara, Toshifumi Shimizu, et al. Chromospheric lyman-alpha spectro-polarimeter (clasp). In Space Telescopes and Instrumentation 2012: Ultraviolet to Gamma Ray, volume 8443, page 84434F. International Society for Optics and Photonics, 2012.
- Shin-nosuke Ishikawa, Masahito Kubo, Yukio Katsukawa, Ryouhei Kano, Noriyuki Narukage, Ryohko Ishikawa, Takamasa Bando, Amy Winebarger, Ken Kobayashi, Javier Trujillo Bueno, et al. Clasp/sj observations of rapid time variations in the ly α emission in a solar active region. The Astrophysical Journal, 846(2):127, 2017.
- Ken Kobayashi, Amy R Winebarger, Sabrina Savage, Patrick Champey, Peter N Cheimets, Edward Hertz, Alexander R Bruccoleri, Jorg Scholvin, Leon Golub, Brian Ramsey, et al. The marshall grazing incidence x-ray spectrometer (magixs). In Space Telescopes and Instrumentation 2018: Ultraviolet to Gamma Ray, volume 10699, page 1069927. International Society for Optics and Photonics, 2018.
- Ken Kobayashi, Jonathan Cirtain, Amy R
 Winebarger, Kelly Korreck, Leon Golub, Robert W
 Walsh, Bart De Pontieu, Craig DeForest, Sergey
 Kuzin, Sabrina Savage, et al. The high-resolution
 coronal imager (hi-c). Solar Physics, 289(11):
 4393-4412, 2014.
- Amy R Winebarger, Bart De Pontieu, Chun Ming Mark Cheung, Juan Martinez-Sykora, Viggo H Hansteen, Paola Testa, Leon Golub, Sabrina L Savage, Jenna Samra, and Katharine Reeves. Unfolding overlappogram data: Preparing for the cool-aid instrument on hi-c flare. AGUFM, 2019:SH33A-06, 2019.
- Charles Kankelborg, Philip Judge, Amy Winebarger, Ken Kobayashi, and Roy Smart. Vuv spectroscopy of the sun as a star. In *Solar Physics Department*. Montana State University, 2017.

- TN Woods, FG Eparvier, R Hock, AR Jones, D Woodraska, D Judge, L Didkovsky, J Lean, J Mariska, H Warren, et al. Extreme ultraviolet variability experiment (eve) on the solar dynamics observatory (sdo): Overview of science objectives, instrument design, data products, and model developments. In *The solar dynamics observatory*, pages 115–143. Springer, 2010.
- H Peter. The chromosphere in coronal holes and the quiet-sun network: An he i (584 å) full-disk scan by sumer/soho. *The Astrophysical Journal Letters*, 522(1):L77, 1999.
- Klaus Wilhelm, W. Curdt, E. Marsh, Udo H. Schuehle, Philippe Lemaire, Alan H. Gabriel, Jean-Claude Vial, Michael Grewing, Martin H.C. Huber, S. D. Jordan, Arthur I. Poland, Roger J. Thomas, Mikhael Kuehne, J. Gethyn Timothy, Donald M. Hassler, and Oswald H. W. Siegmund. Some design and performance features of SUMER: solar ultraviolet measurements of emitted radiation. In Silvano Fineschi, editor, X-Ray and EUV/FUV Spectroscopy and Polarimetry, volume 2517, pages 2 11. International Society for Optics and Photonics, SPIE, 1995. doi: 10.1117/12.224908. URL https://doi.org/10.1117/12.224908.
- Craig J Sansonetti, F Kerber, Joseph Reader, and Michael R Rosa. Characterization of the farultraviolet spectrum of pt/cr-ne hollow cathode lamps as used on the space telescope imaging spectrograph on board the hubble space telescope. The Astrophysical Journal Supplement Series, 153(2): 555, 2004.
- Genevieve D. Vigil, Amy R. Winebarger, Laurel Rachmeler, Ken Kobayashi, Nicolas Donders, and Charles Kankelborg. [abstract] relative radiometric calibration for full-sun ultravioletrocket spectrograph. In Space Telescopes and Instrumentation 2018: Ultraviolet to Gamma Ray, volume 11444, page 136. SPIE, 2020.

IAC-20,A7,3,7,x57894 Page 8 of 8